Single-end Protection Scheme Based on Transient Power Waveshape for Hybrid HVDC Transmission Lines

Feiyang Dai, Zexin Zhou, and Xingguo Wang

***Abstract*—The recent in-depth development of hybrid high-voltage direct current (HVDC) transmission systems poses looming adaptability challenges to protection. The various and disparate direct current (DC) transmission topologies can profoundly affect the operating characteristics of DC transmission networks, which result in the lack of performance of conventional DC protection schemes in such topologies. This significantly limits the application of hybrid HVDC technologies. This paper proposes a single-end protection scheme based on the transient power waveshape for fast and sensitive detection and classification of different types of DC faults in hybrid HVDC transmission lines. The fault characteristics and their causes under different fault conditions are analyzed in detail with a pre-introduced linearized transient model of a hybrid HVDC transmission system, demonstrating that the formation of the fluctuation characteristics of local measurements is mainly determined by the buffering and absorption effects of lumped-parameter reactors on transient traveling-wave (TW) energy. Simulation results verify the sensitivity, rapidity, reliability, and anti-interference ability of the proposed scheme when applied to hybrid HVDC transmission lines. Furthermore, it is confirmed that the proposed scheme is adaptable to symmetric voltage-sourced converter (VSC) and conventional line-commutated converter (LCC) based HVDC transmission lines.**

***Index Terms*—High-voltage direct current (HVDC) transmission system, line protection, travelingwave (TW), line-commutated convrter, floating threshold.**

I. Introduction

HYBRID high-voltage direct current (HVDC) transmission technology is the product of the complementary advantages of voltage-sourced converter (VSC) based direct current (DC) transmission technology and conventional line-commutated converter (LCC) based DC transmission technology, which aims to extend the networking flexibility of DC transmission systems. Hybrid HVDC systems typically have superior control performance, a relatively large transmission capacity, a long transmission distance, and high stability. The industry has successfully designed and improved a series of hybrid HVDC transmission systems with both VSCs and LCCs simultaneously [1], [2], which are often particularly suitable for solving specific engineering problems or improving the robustness of local DC grids [3], [4]. There have been many hybrid DC projects in China such as the Kun-Liu-Long and Baihetan-Jiangsu projects, which show the broad application prospects of hybrid HVDC technologies.

Hybrid HVDC transmission systems are generally associated with a changeable network topology, dynamic response features, a low inertia, and damping characteristics. These inherent features of hybrid HVDC transmission systems require primary line protection to further improve their "four performance criteria" compared with conventional DC protection, and have good adaptability when applied to line terminals with different structures [5]. However, existing HVDC transmission line protection schemes in operation based on a differential undervoltage or the arrival of a travelingwave (TW) cannot meet the increasing requirements of sensitivity or reliability, which leads to the lack of performance of these existing protection schemes. This becomes an important factor that restricts the application of hybrid DC transmission technologies [6], [7]. Furthermore, numerous simulations and on-site wave recordings have shown that the fault characteristics experienced by line terminals vary broadly in terms of the structures of these terminals [8], [9], significantly increasing the difficulty and complexity of designing primary line protection schemes.

The industry has now redesigned various line protection schemes for HVDC transmission lines. Many of these achievements excel in algorithm simplicity and performance, but most of them are for specific transmission scenarios [10]-[13], and hence, it might be challenging to directly apply them to hybrid DC transmission systems regarding relay setting and coordination. These more hybrid-focused protection schemes are primarily based on the use of complex algorithms to separate electrical quantities in specific frequency bands, and thus, might not satisfy the strict operation speed requirements of HVDC systems. In [14], a single-end dual-tree complex wavelet transform (DTCWT) based relay prin-

Manuscript received: June 14, 2022; revised: September 19, 2022; accepted: November 7, 2022. Date of CrossCheck: November 7, 2022. Date of online publication: November 28, 2022.

This work was supported by the Science and Technology Project of State Grid Corporation of China "Research on ultra-high-speed protection and fault isolation technology of transmission lines in DC power grid with different structures" (No. 5100-202155030A-0-0-00).

F. Dai (corresponding author), Z. Zhou, and X. Wang are with the China Electric Power Research Institute Co., Ltd., Beijing, China, and Z. Zhou and X. Wang are also with the State Key Laboratory for Power Grid Safety and Energy Conservation, Beijing, China (e-mail: bfg10k@sina.com; zhouzx@epri.sgcc.com.cn; wangxingguo@epri.sgcc.com.cn).

DOI: 10.35833/MPCE.2022.000290

ciple is proposed to detect and identify internal faults with a transient resistance of up to 500 Ω for hybrid transmission lines. However, its corresponding algorithm is too complicated and may not be practical in ultrahigh-speed HVDC protection scenarios. Reference [15] proposes a protection scheme using frequency-dependent transient energy separation algorithms to identify and distinguish faults. It is less relevant to the terminal structure but uses a complex mathematical algorithm that requires a long time window. Reference [16] focuses on hybrid DC distribution networks with much shorter line lengths, in which the proposed scheme can only reflect fault signatures that are very different from those of hybrid HVDC transmission systems. In general, there is an urgent need for high-performance protection schemes that can adapt to various HVDC transmission scenarios, particularly hybrid HVDC transmission systems.

Given the lack of highly adaptive protection solutions for hybrid HVDC transmission lines, a transient-power-based single-end protection scheme is proposed in this paper as an ultrafast method with broad applicability for detecting, distinguishing, and identifying line faults in hybrid HVDC transmission systems. The strong absorption and buffering effects exerted by lumped-parameter reactors at the line terminals on transient TWs are quantitatively explored through detailed analyses of the fault characteristics in such systems. The difference in the transient power variation is widely utilized to form a group of composite protection subunits that can cover fault detection and location and prevent relay maloperation in different scenarios. The proposed scheme can adapt well to hybrid HVDC transmission systems, conventional LCC-HVDC transmission systems, and flexible VSC-HVDC transmission systems with outstanding practical engineering value.

II. Hybrid HVDC Transmission System Model and Its Linearization

The strict speed requirements for HVDC transmission line protection indicate that an analysis of the fault-induced forward TW signal is preferable as the main principle for designing a practical primary HVDC transmission line protection scheme. Suppose that the analysis of the fault-induced TW waveform is confined within 1-2 ms after the first arrival of the TW. Then, HVDC network structures with considerable time delays can be reasonably simplified to locally linearize the DC power grid. Subsequently, the corresponding transient local network satisfies the superposition theorem and can be used to conveniently and quantitatively analyze the TW waveform. This paper employs linearization according to standard HVDC simplification schemes [17]-[20].

A. Overall Model

The hybrid HVDC transmission system in point-to-point end-to-end mode, as shown in Fig. 1, is modeled using the real-time digital simulation system (RTDS) platform, where L_{dc} is the lumped-parameter reactor; U_R, I_R, U_I, and I_I are the raw measurements at the VSC and LCC ends of the positive pole; U_{dc} is the DC load voltage; and F_1-F_7 represent typical fault locations. We define R_v, L_v, and C_v as the equivalent resistance, inductance, and capacitance of these converters, respectively, and ignore the influence of alternating current (AC) systems. The parameters of the VSC and transmission lines are listed in Appendix A Table AI, while the parameters of the LCC and DC filter are listed in Appendix A Table AII. Most of the subsequent analyses will be based on this model.

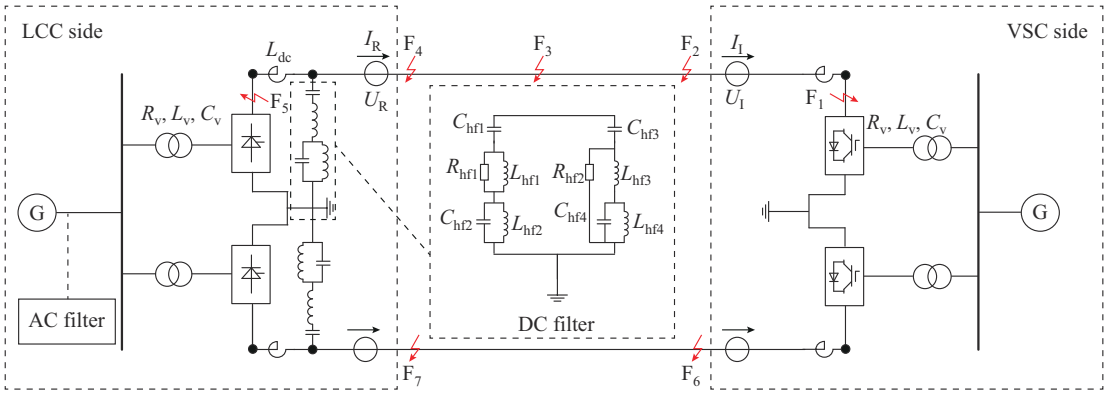

Fig. 1. Diagram of hybrid HVDC transmission system.

B. Simplification of Converter

VSCs and LCCs generally have prominent time-delay characteristics and might not take noticeable actions until the operation of related line protections. This paper considers that the control logic of the converters does not respond within 2 ms after the first arrival of the fault-induced TW and treats the parameters of these converters as constants.

C. Simplification of Line

According to the derivation of the external characteristics of a distributed transmission line segment, a lossless transmission line can be regarded as a lumped-parameter resistor when a TW propagates through it. Defining its resistance as Z_c, the propagation process of a TW can be briefly expressed as:

$$U_q\left(t_p-\frac{x}{v}\right)=Z_c I_q\left(t_p-\frac{x}{v}\right) \tag{1}$$

where U_q and I_q are the front voltage and current TWs, respectively; t_p is the propagation time; x is the distance traveled by the TWs; and v is the maximum velocity of the TW. Considering the influence of the line loss and dispersion on the fault characteristics, the model adopts a lossless line for an alternative analysis.

III. Analysis on Fault Characteristics of Hybrid HVDC Transmission Lines

When a line fault occurs, a transient equivalent excitation $-\Delta U_{dc}\varepsilon(t)$ will be connected in parallel to the fault point and provide the initial TW signal U_{src} to both sides of the line. According to the boundary conditions of the fault location, the initial moduli of the forward TW are expressed in (2) and (3), where (2) is for single-pole fault; and (3) is for dual-pole fault [20].

$$U_{src}(t)=\frac{-\Delta U_{dc}Z_{c1}}{(Z_{c1}+Z_{c0})+4R_g}\varepsilon(t) \tag{2}$$

$$U_{src}(t)=\frac{-\Delta U_{dc}Z_{c1}}{Z_{c1}+R_g}\varepsilon(t) \tag{3}$$

where R_g is the transient grounding resistance; and Z_{c1} and Z_{c0} are the differential- and common-mode wave impedances of the transmission line, respectively. The values for the modulus can be obtained via local polar measurements and utilized to eliminate the influence of the interpole mutual impedance [21]. Equations (2) and (3) indicate that the waveform of the initial forward TW is step-shaped, which significantly differs from the waveform of the TW measured at the line terminals. This is because the fault-induced TWs generated by the equivalent excitation should first form the incident wave of the local system after being refracted and reflected. Subsequently, the incident wave can form a voltage drop and TW current on the remnant system behind the local measurement point, and can be reflected in the measured electrical quantities. These two conclusions constitute the basis of an analysis on the fault characteristics of hybrid HVDC transmission lines. The following definitions are provided to clarify the references to the variables in the analysis process.

1) In this paper, the protection schemes based on the characteristics of transient electric power are designed, which involve the analysis of the waveforms of measured voltage, current, and power at the local terminals. Therefore, $F\in(U,I,P)$ is defined to represent the voltage, current, and power, respectively; F_B is defined as the incident TW of the local transient system; and F_y is defined as the raw local measurements. The transient quantity F_m is determined by:

$$F_m=F_y-F_N \tag{4}$$

where F_N is the rated values of these quantities.

2) The lumped-parameter components at the line terminals, mainly referring to the smoothing reactors, current-limiting reactors, and DC filters, are defined as "line boundaries". The area between the line boundaries of a transmission line is defined as the primary protection zone.

A. Analysis on Refraction Characteristics of Boundary

Once the topology of a local line terminal is given, the Thevenin equivalent circuit of the terminal can be drawn to obtain its system of state equations for quantitative analysis. Such a circuit structure will be independent of the fault conditions, where the difference remains in the incident voltage of TW U_B. U_B will be equal to U_{src} after an internal fault occurs; however, under external fault conditions, the initial front voltage of TW U_{src} is first refracted into a refracted wave U_F through the opposite line boundary. Then, U_F becomes the incident wave of the residual Thevenin equivalent circuit, whose topology is identical to that when an internal fault occurs. Therefore, U_B must first be derived through an analysis on the refraction characteristics of the boundaries.

1) Refraction Characteristics at VSC End

The line boundaries of typical VSC terminals mainly refer to the current-limiting reactors, whose refraction features can be obtained from Fig. 2, where F_F is the refracted TW induced by F_B.

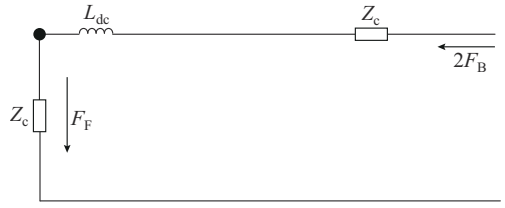

Fig. 2. TW Thevenin equivalent circuit of line boundary at VSC end.

The state equation of the equivalent circuit in Fig. 2 can be obtained using the fundamental circuit theorem:

$$2U_B(s)=(sL_{dc}+2Z_c)I_y(s) \tag{5}$$

$$U_F(s)=2U_B(s)-(sL_{dc}+Z_c)I_y(s) \tag{6}$$

The general solution to the system of linear differential equations can be obtained using an inverse Laplace transform (ILT) as:

$$U_F(t)=2|U_{src}|(1-e^{-2Z_c t/L_{dc}}) \tag{7}$$

$$I_F(t)=-2|U_{src}|(1-e^{-2Z_c t/L_{dc}})/Z_c \tag{8}$$

Equations (5) and (6) indicate that U_F and I_F are logarithmic wave heads with a lower steepness and amplitude than those of F_b. This is mainly because their transient TW energy has been significantly buffered by L_{dc}, as the reactor current cannot change abruptly. Figure 3 shows the comparison of the TW waveforms at the line boundary at the VSC end, including the fluctuations in the analytical waveforms, their simulated counterparts of U_F and I_F, and the transient power of the refracted TW after being buffered and attenuated by the VSC terminal line boundary. It can be observed that the simulation results are consistent with the analytical results.

2) Refraction Characteristics at LCC End

The line boundary of the LCC terminal comprises a smoothing reactor and DC filter. Considering the relatively high order of the local system increased by the DC filter, an equivalent DC filter with only its $6^{th}/12^{th}$ filters preserved is studied in isolation using Fig. 4 and (9)-(11) for the sake of simplicity.

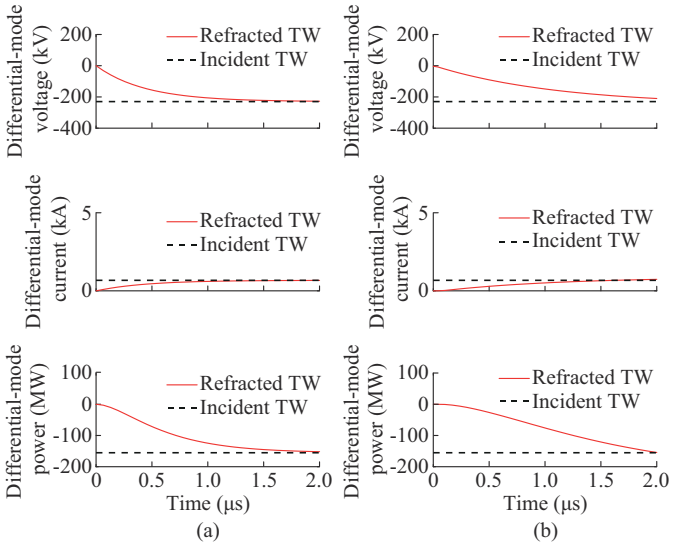

Fig. 3. Comparison of TW waveforms at line boundary at VSC end. (a) Analytical waveform. (b) Simulated waveform.

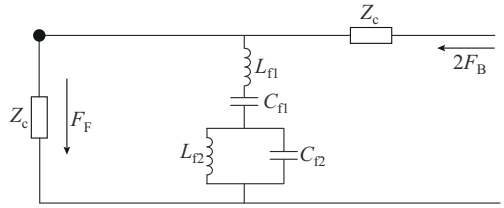

Fig. 4. TW Thevenin equivalent circuit of LCC-side line boundary.

$$X(s)=sL_{f1}+1/sC_{f1}+1/(s^2C_{f2}L_{f2}+1) \tag{9}$$

$$I_m(s)=2U_B(s)(X(s)+Z_c)/(2Z_cX(s)+Z_c^2) \tag{10}$$

$$U_m(s)=2U_B(s)-I_m(s)Z_c \tag{11}$$

$I_m(s)$ can be expressed by a fraction as:

$$I_m(s)=N(s)/D(s) \tag{12}$$

The denominator $D(s)$ contains five eigenvalues, all of which are complex, except for $s=0$, which is injected by the step transient fault excitation. However, if the coefficients of element s with different orders in $D(s)$ are referred as a_4, a_3, a_2, a_1, a_0 in descending order, the general form of the four unknown eigenvalues can be obtained using basic solution processes for univariate quartic equations as:

$$J=\frac{1}{2}\sqrt{\frac{a_3^2}{2a_4^2}-\frac{4a_2}{2a_4}-\Delta\pm\frac{-\frac{a_3^3}{a_4^3}+\frac{4a_3a_2}{a_4^2}-\frac{8a_1}{a_4}}{4\sqrt{\frac{a_3^2}{4a_4^2}-\frac{2a_2}{3a_4}+\Delta}}} \tag{13}$$

$$R=-\frac{a_3}{4a_4}\pm\frac{1}{2}\sqrt{\frac{a_3^2}{4a_4^2}-\frac{2a_2}{3a_4}+\Delta} \tag{14}$$

$$s=R\pm J \tag{15}$$

where Δ is an intermediate defined by a_0-a_4, given by the Ferrari method to simplify the mathematical expression. By substituting the relative parameters into (13) - (15), it is known that the value of the expression underneath the square-root sign in the equation for J is always less than 0. In contrast, R is significantly smaller than the absolute value of J, which indicates that the refracted TW is characterized by the superposition of dual-frequency attenuating oscillation waveforms with minor amplitudes. Furthermore, the eigenvalue $s=0$ causes F_F to be near the steady-state value of the incident TW, showing a step waveform. The time-domain solutions of F_F can be expressed via an ILT, whose analytical waveform is shown in Fig. 5:

$$K_i=\left.\frac{N(s)}{D'(s)}\right|_{s=s_i} \quad i=1,2,3,4 \tag{16}$$

$$I_m(t)=2|K_1|\cos(\omega_1 t+\theta_1)+2|K_3|\cos(\omega_3 t+\theta_3)+\frac{\Delta U_{dc}}{Z_c}\varepsilon(t) \tag{17}$$

$$U_m(t)=2|U_{src}|\varepsilon(t)-I_y(t)Z_c \tag{18}$$

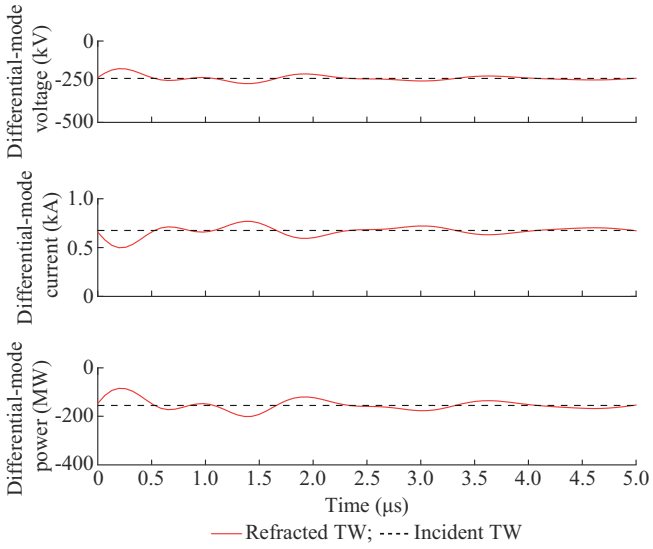

Fig. 5. Refraction characteristics of DC filter.

Figure 5 shows that typical DC filters absorb little TW energy; their L-C resonant couplings mainly inject high-frequency harmonics into the faulty line and cause minor distortions in the local relay measurements. Such external characteristics of DC filters for fault-induced TW signals are easy to understand because the standard 6th/12th- and 12th/24th/36th-tuned DC filters are bandpass filters for specific harmonics. They will show a high-resistance state to DC-component-dominated fault-induced TWs, which has been widely proven [22]. This allows most energies of the transient TW to be directly refracted into the parallel resistor branch.

The characteristics of the LCC-side line boundary can now be discussed on the above basis. The fault-induced initial front TW produced by the transient excitation is first buffered into a refracted wave (as shown in Fig. 5) by the smoothing reactor of the line boundary. Its system of state equations can then be obtained by substituting F_F into (6) and analyzed by the integral convolution (IC) method:

$$I_m(t)=\mathcal{L}^{-1}\left(\frac{1}{sL_{dc}+2Z_c}\right)*\mathcal{L}^{-1}\left(\frac{|U_{src}|}{s}\frac{X(s)+Z_c}{2Z_cX(s)+Z_c^2}\right) \tag{19}$$

$$U_{\mathrm{m}}(t)=2U_{\mathrm{B}}(t)-I_{\mathrm{m}}(t)Z_{\mathrm{c}} \tag{20}$$

Because the second term on the right-hand side of (19) is approximately a step wave, the refracted wave will maintain its waveform features to a great extent when propagating through the DC filter according to the concepts of convolution and integration of the IC method. Therefore, the LCC-side line boundary mainly reflects the buffering effect of its smoothing reactor, similar to the VSC-side line boundary.

The simulation results for U_{F} and I_{F} and the transient power of the refracted TW induced by the LCC-side line boundary are compared with the individual results at the VSC side, as shown in Fig. 6. It can be observed that the LCC-side line boundary has similar effects on the incident TWs passing through it as the VSC-side line boundary, producing F_{F} with clear logarithmic wave heads.

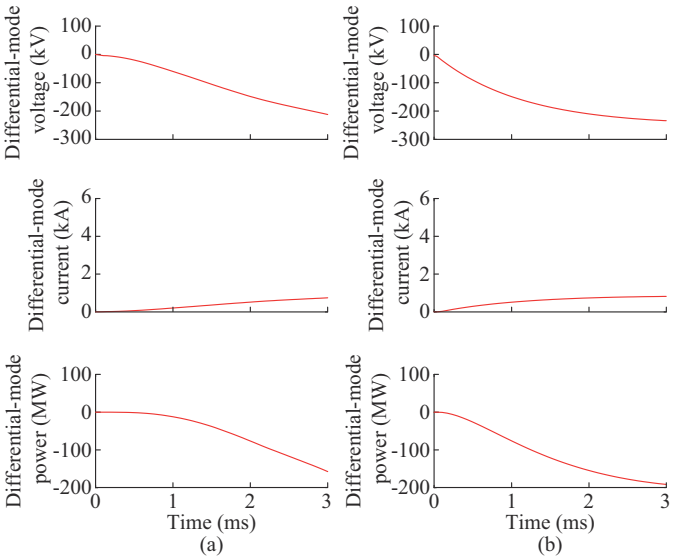

Fig. 6. Comparison of refracted TW waveforms on both sides. (a) LCC-side waveforms. (b) VSC-side waveforms.

B. Analysis on Fault Characteristics at LCC End

The TW Thevenin equivalent circuit of conventional LCC-side line boundaries, as shown in Fig. 7, can be used to analyze the fault characteristics of the relay measurements on the LCC side.

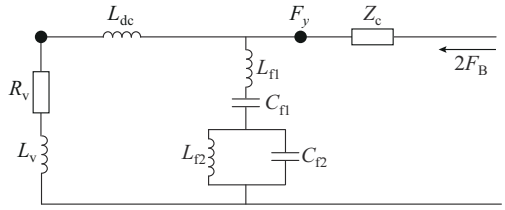

Fig. 7. TW Thevenin equivalent circuit of conventional LCC-side line boundaries.

To satisfy the fundamental laws of Thevenin's theorem in the TW realm, a current TW must first be refracted by the DC-filter branch to satisfy the law of loop current analysis; however, a voltage TW should be studied considering the valve and filter branches together to fulfill the law of node voltage analysis. The state equation for the measured voltage is expressed via (5) as:

$$X(s)=sL_{\mathrm{f1}}+\frac{1}{sC_{\mathrm{f1}}}+\frac{1}{s^2C_{\mathrm{f2}}L_{\mathrm{f2}}+1} \tag{21}$$

$$U_{\mathrm{m}}(s)=2U_{\mathrm{B}}(s)\left[1-\frac{X(s)+sL_{\Sigma}}{(sL_{\Sigma}+Z_{\mathrm{c}})X(s)+sL_{\Sigma}Z_{\mathrm{c}}}\right] \tag{22}$$

where L_{Σ} is the sum of L_{dc} and L_{v}. Depending on the structure of the incident wave U_{B} (which is determined by the fault location, as shown in Section III-A), (22) will have eigenvalues with different forms and influence the waveshapes of the local relay measurements.

1) When an internal fault occurs, U_{B} is equal to $2|U_{\mathrm{src}}|/s$. An eigenvalue of 0 is injected into $D(s)$ by the arithmetic element $1/s$ of U_{B}, causing local measurements to abruptly change during the arrival of the front TWs. Meanwhile, the *R-L* parallel branch of the LCC provides a large negative real root, causing local measurements to decline in a logarithmic manner.

2) When an external fault occurs, U_{B} is given by (18). This will inject an additional negative real root of $-Z_{\mathrm{c}}/L_{\Sigma}$ into $D(s)$, further weakening the steepness of the local measurements.

Figure 8 shows the simulation results for the characteristics of the fluctuation in the local relay measurements when a metallic pole-to-ground (PG) fault occurs at different fault locations. It can be observed that I_{m} can abruptly vary during the arrival of the TW because of the distortion in the DC filter, whereas U_{m} cannot. The fluctuation in the transient power in the case of an external fault is much more moderate than that in the case of an internal fault.

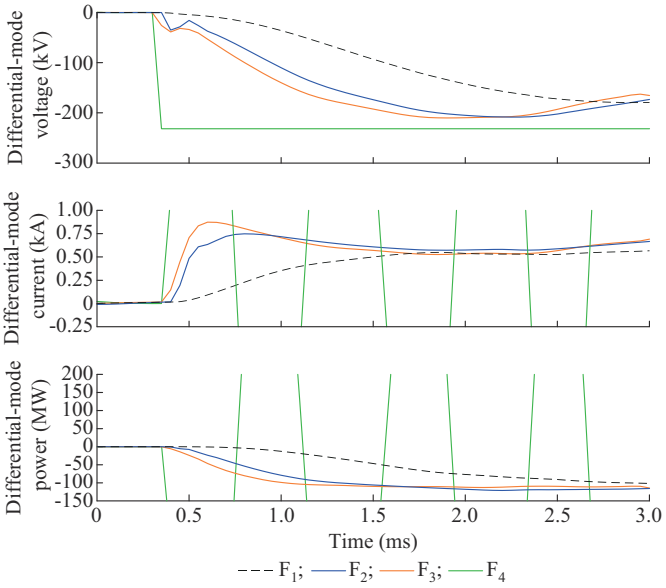

Fig. 8. Waveforms of transient measurements on LCC side.

C. Analysis on Fault Characteristics at VSC End

The TW Thevenin equivalent circuit in Fig. 9 can be used to analyze the fault characteristics of the relay measurements on the VSC side.

The state equation of U_{m} can be written as:

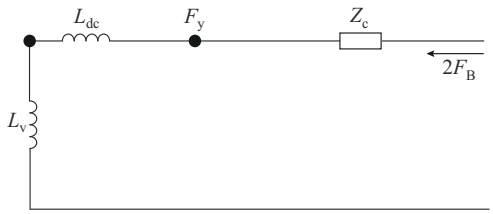

Fig. 9. TW Thevenin equivalent circuit of VSC-side line boundaries.

$$[1/(sC_v)+sL_\Sigma+Z_c]I_m(s)=2U_B(s) \tag{23}$$

$$U_m(s)=2U_B(s)-Z_cI_m(s) \tag{24}$$

Owing to the high damping of the series resistance Z_c, the relatively small valve capacitance C_v is ignored here because it has little influence on the numerical features of the eigenvalues. Equation (5) shows that the waveshape of U_m is still heavily dependent on the structure of the incident wave U_B, which needs to be discussed in different fault scenarios.

1) During an internal fault, U_B will be equal to $2|U_{src}|/s$. The general solution of (23) and (24) can then be derived as:

$$U_m(t)=-2|U_{src}|e^{-Z_ct/L_{dc}} \tag{25}$$

$$I_m(t)=2|U_{src}|(1-e^{-Z_ct/L_{dc}})/Z_c \tag{26}$$

U_m suddenly drops by $-2|U_{src}|$ when the front TW arrives and then gradually increases in a logarithmic manner as the TW charges the VSC-side, similar to the step response of a typical first-order inductor. In contrast, I_m increases in a logarithmic manner since the beginning of the arrival of the front TW. The transient power P_m in this scenario would fluctuates in a similar manner as U_m does.

2) During an external fault, U_B will be equal to (7). If the LCC-side line boundary is treated as a lumped-parameter reactor on the basis of Section III-A, the analytical forms of U_m and I_m at this time would be expressed as:

$$U_m(t)\approx\frac{2|U_{src}|Z_c}{L_{dc}}(e^{-2Z_ct/L_{dc}}-e^{-Z_ct/L_\Sigma}) \tag{27}$$

$$I_m(t)\approx-\frac{2|U_{src}|}{L_{dc}}(1-e^{-Z_ct/L_\Sigma}) \tag{28}$$

Compared with those in (25) and (26), the transition process of U_m is considerably prolonged with no abrupt changes and a much lower steepness. Thus, P_m has a much smoother and moderately curved trend.

3) In the particular case where an internal fault occurs at F_4 in Fig. 1, the transient excitation will directly impact the LCC-side line boundary and charge the DC filter before TWs are produced. This weakens and distorts the waveshapes of the local measurements to some extent.

Figure 10 shows the simulated waveforms of transient measurements at the VSC end under metallic PG faults for different fault locations, from which the conclusions of the analysis are demonstrated to be consistent with the experimental results.

D. Summary

In conclusion, the lumped-parameter reactors with line boundaries have a strong buffering effect on the signals with abruptly changing features, which aligns with their design objectives and provides favorable conditions for fault identification. The following general conclusions can be drawn from Figs. 8 and 10.

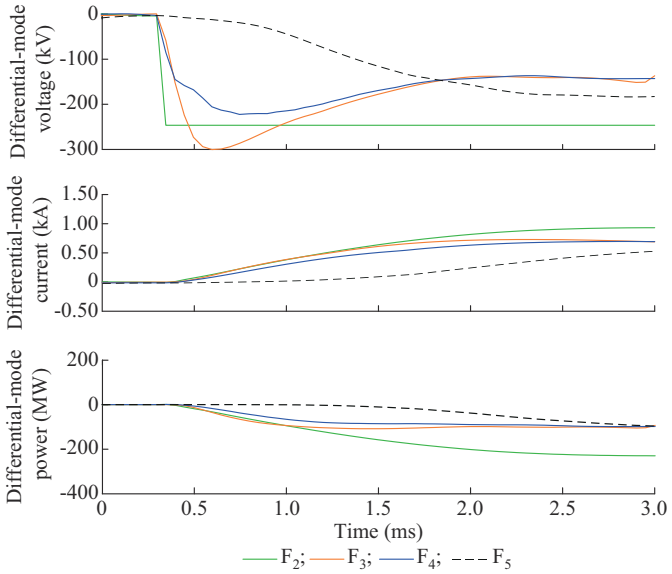

Fig. 10. Simulated waveforms of transient measurements at VSC end.

1) When an internal fault occurs, the VSC-side line boundary allows U_y to abruptly change while buffering and smoothing I_y. In contrast, the LCC-side line boundary allows I_y to abruptly change while weakening the steepness of U_y. This means that specific conventional protection schemes based on the rate of change in the current/voltage are inapplicable to both terminals of a hybrid HVDC transmission system.

2) As DC filters are bandpass filters and show a high-resistance state to TW signals, the line boundaries of both terminals approximately act as reactors when TWs pass through them. Hence, the variation in the transient TW power shows a similar trend at both terminals of the hybrid HVDC transmission system. It is noted that the topology of the DC filters does not influence the general features of the local transient power as long as they are in a high-resistance state relative to the DC wave components.

IV. Protection Scheme Based on Transient Power Waveshape

The proposed protection scheme based on transient power waveshape focuses on hybrid HVDC transmission systems with both VSC and LCC terminals and consists of four subunits. The following subsections discuss each subunit in detail.

A. Differential Transient TW Power Based Fault Identification Subunit

This subunit is the core function element of the proposed protection scheme, realizing fault detection and rough location. Its core ideas include the following aspects.

1) The transient TW power reflects the combined fluctuations in the waveshapes of the measured voltage and current and can be utilized to sensitively distinguish internal high-re-

sistance grounding faults.

2) The transient TW power of the VSC/LCC terminals shows similar and significant variation trends, which is ideal for fault location.

However, it is noted that the fault resistance could severely affect the magnitude of the TW waveform while imposing minor impacts on its waveshape. Therefore, this protection unit utilizes the difference rather than the amplitude of the measured transient TW power. The fault identification criterion is constructed on the aforementioned basis as:

$$\Delta P_{\mathrm{m}}(t+t_0)=P_{\mathrm{m}}(t+t_0)-P_{\mathrm{m}}(t+t_0-1) \tag{29}$$

$$|\Delta P_{\mathrm{m}}(t+t_0)|>k_1(t)P_{\mathrm{Lset}} \tag{30}$$

$$t<2 \tag{31}$$

where t_0 is the startup time of the protection; t is the elapsed time; ΔP_{m} is the difference in P_{m}; and P_{Lset} is a predefined action threshold set according to the maximum local transient TW power difference within 0.5 ms when an external metallic PG fault occurs at F_5. The floating threshold factor k_1 is defined as:

$$k_1(t)=\begin{cases}1 & t\le t_{\mathrm{a}}\\ k_2(t-t_{\mathrm{a}})+1 & t_{\mathrm{a}}<t\le t_{\mathrm{b}}\\ k_3(t-t_{\mathrm{b}})+k_2(t_{\mathrm{b}}-t_{\mathrm{a}})+1 & t>t_{\mathrm{b}}\end{cases} \tag{32}$$

where k_2, k_3, t_{a}, and t_{b} are the coefficients that describe the shape of the floating threshold. t_{a} can be experimentally set under the condition that an internal metallic PG fault occurs at the opposite terminal of the line, which is expressed as:

$$\Delta P_{\mathrm{m}}(t_{\mathrm{a}}')-\Delta P_{\mathrm{m}}(t_{\mathrm{a}}'-1)\le 0 \tag{33}$$

$$\Delta P_{\mathrm{m}}(t_{\mathrm{a}})<0.5\Delta P_{\mathrm{m}}(t_{\mathrm{a}}'-1) \tag{34}$$

That is, the protection unit will first locate the time point t_{a}' when the transient TW power $\Delta P_{\mathrm{m}}(t)$ begins to decline, and then complete the abrupt variation process of $P_{\mathrm{m}}(t)$ by the time point t_{a} when $\Delta P_{\mathrm{m}}(t)$ decreases to less than half of $\Delta P_{\mathrm{m}}(t_{\mathrm{a}}')$. k_2, k_3, and t_{B} can be set according to the following formulas under the same fault condition in which t_{a} is set:

$$f(c)=\Delta P_{\mathrm{m}}(c) \tag{35}$$

$$t_{\mathrm{b}}\in\underset{t_0<c<t_0+1.5}{\arg\max}\, f(c) \tag{36}$$

$$k_2=\frac{\Delta P_{\mathrm{m}}(t_{\mathrm{b}})-\Delta P_{\mathrm{m}}(t_{\mathrm{a}})}{t_{\mathrm{b}}-t_{\mathrm{a}}} \tag{37}$$

$$k_3=2k_{\mathrm{a}} \tag{38}$$

This protection unit will find the time point t_{b} when $\Delta P_{\mathrm{m}}(t)$ reaches its maximum value within 1.5 ms after the protection starts; then, the slope between $\Delta P_{\mathrm{m}}(t_{\mathrm{b}})$ and $\Delta P_{\mathrm{m}}(t_{\mathrm{a}})$ is set as k_2. k_3 is set mainly to prevent maloperation; thus, a large value is preferred. In this paper, its value is $2k_2$. A curve of the variation in the floating threshold k_1 can be drawn according to (32) - (38), which is shown in Fig. 11.

The purpose of k_1 is to improve the performance of the unit. The time interval [0, t_{a}] of k_1 can reasonably lower the action setting shortly after the protection starts, thereby providing a sensitivity boost to the unit. This is because the development of the local fault characteristics induced by external faults is initially delayed and mitigated owing to the buffering effect of the line boundaries. This interval can also eliminate the effects of bipolar coupling. Over time, the local transient power may eventually develop specific symbolic fluctuation characteristics under internal fault conditions, resulting in possible maloperation of the protection. The time interval [t_{a}, t_{b}] of k_1 can increase the action threshold to prevent maloperation, thereby improving the reliability and selectivity of the subunit. If the subunit cannot operate beyond the point t_{b}, the protection unit renders the fault an external fault and sharply raises the threshold to secure the reliability of the protection.

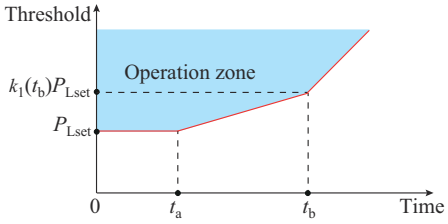

Fig. 11. Variation in floating threshold k_1.

Taking the VSC terminal in Fig. 1 as an example, Fig. 12 shows the results of application of differential transient TW power based fault identification unit during metallic PG faults of different locations. It can be observed that the trend in the curve of $\Delta P_{\mathrm{m}}(t)$ is consistent with the theoretical analysis, given that $|\Delta P_{\mathrm{m}}(t)|$ can meet the floating threshold only when internal faults occur.

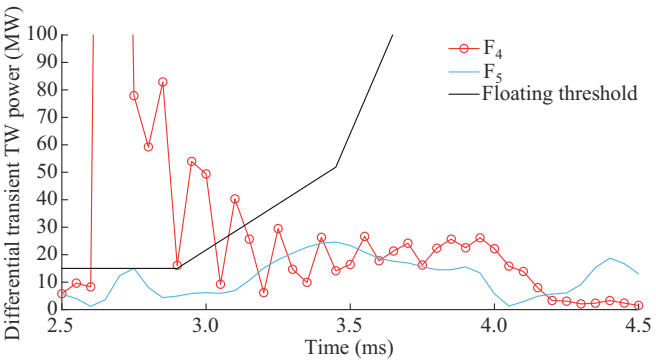

Fig. 12. Results of application of differential transient TW power based fault identification unit.

B. Maloperation Prevention Subunit for Lightning Disturbance (LD)

A major deficiency of the fault identification subunit is that it cannot reliably distinguish faults from other types of instantaneous disturbances. These instantaneous disturbances, especially LD, can induce pulse features in the local measurements, which may be confused with the waveshapes of the local measurements during the arrival of the fault-induced TW, and can cause potential incidents of maloperation. However, when struck by such LD, the abrupt variations in the local measurements often last for less than 0.1 ms, and it generally takes less than 1 ms for these measure-

ments to decline and stabilize at their rated steady-state values. Therefore, the waveshape of $P_m(t)$ would show a sharp yet unsustainable trend in variation, and clearly contrast with that in the case of internal faults. For instance, Fig. 13 shows the waveforms of the local measurements on the LCC side during an LD at F_2. It can be concluded that I_m and P_m induced by the LD have pulsed waveshapes, typically with a transient process that lasts for only hundreds of microseconds but peaks at tens of times the load current.

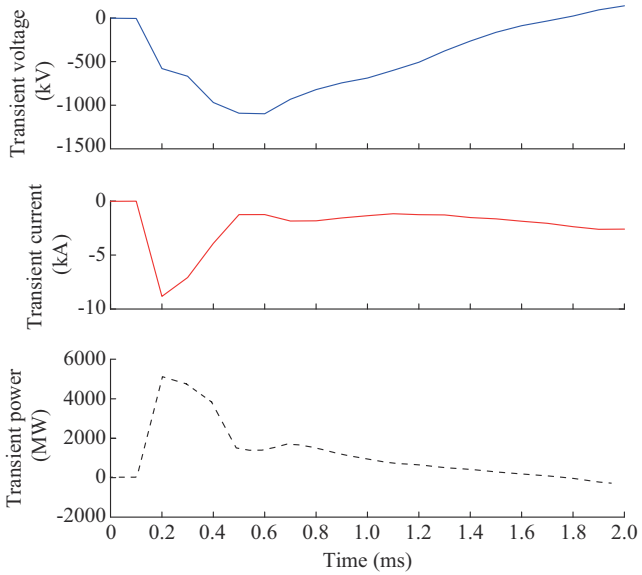

Fig. 13. Waveforms of local measurements on LCC side during LD at F_2.

The following protection criteria are designed as the core criteria of the maloperation prevention subunit:

$$D = \max\{|P_m(t_0)|, |P_m(t_0+1)|, \ldots, |P_m(t+t_0)|\} \tag{39}$$

$$D_A = \sum_{t=0}^{t_{set}} \frac{|P_m(t+t_0)|}{D} > P_{Tset} \tag{40}$$

where t_{set} is the upper limit of the operation time (OT) of the criteria; D is the maximum local transient power P_m since the protection starts; D_A is the accumulation of the ratio of absolute P_m to D; and P_{Tset} is the operation threshold, which is set according to the OT demands of specific hybrid HVDC projects but is higher than the maximum local ΔP_m in the worst internal LD cases. According to the fluctuation characteristics of $P_m(t)$, the local per-unit transient power during internal LD is close to 1 only for an instant after being impacted because $P_m(t)$ can only increase during this time interval. Then, it decreases to a small value. Hence, D_A will remain at a low level. In contrast, the local per-unit transient power during an internal fault will be 1 at every sampling point, because the waveform of P_m will continuously rise to its steady state, causing the value of D to be equal to that of $P_m(t)$. The discrete integral value D_A will linearly diverge and soon exceed the action threshold.

Figure 14 shows the waveforms of maloperation prevention subunit during actual LD situation. $P_m(t)$ peaks at approximately 0.3 ms and then quickly drops to the vicinity of its load value. P_m of each subsequent sampling point is far less than 1. Therefore, D_A cannot reach the operation threshold.

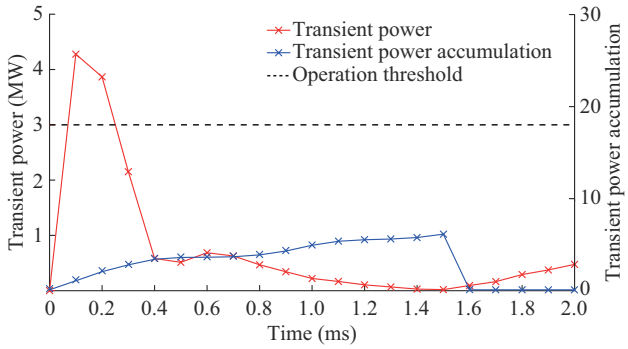

Fig. 14. Waveforms of maloperation prevention subunit during actual LD situation.

Further verification of the performance will be presented in Section V by imposing a typical 2.6/50 μs positive double-exponential lightning disturbance $i_T(t)$ to the simulation model. The function of the disturbance is expressed as:

$$i_T(t) = 50(e^{-1.5\times10^{-8}t} - e^{-1.86\times10^{-6}t}) \tag{41}$$

C. Supplementary Maloperation Prevention Subunits

The subunits mentioned above include high-resistance fault detection, rough location, and lightning disturbance discrimination. However, a complete and practical composite protection scheme requires additional auxiliary function elements.

1) Pole Selection Subunit

The poles of a typical overhead HVDC transmission line share little electrical contact; instead, they are strongly related to the magnetic aspect. However, the magnetic connections between poles could become vital in some scenarios where the modulus measurements of each pole must be utilized to eliminate the influence of mutual inductance. According to the definition of the modulus components, the subunits mentioned above cannot directly determine the faulty pole, which determines the necessity of an additional pole selection criterion.

A pole selection method typically adopts a principle that compares the magnitudes of the measurements, which is relatively mature. The pole selection principle constructed in [22] is adopted in this paper:

$$O(t) = \frac{\sum_{k=t_0}^{t} \Delta i_I(k)}{\sum_{k=t_0}^{t} \Delta i_{II}(k)} \tag{42}$$

where k is the index of the sampling points; and $\Delta i_I(k)$ and $\Delta i_{II}(k)$ are the local differential currents of the positive and negative poles, respectively. When a faulty occurs at one of these poles, the current at the faulted pole must be significantly greater than that at the non-fault pole, which is consistent with the difference in these measurements. Therefore, $O(t)$ complies with the following rules:

1) When positive faults occur, $\Delta i_I(k) \gg \Delta i_{II}(k)$; thus, $O(t) \gg 1$.

2) When negative faults occur, $\Delta i_{\mathrm{I}}(k) \ll \Delta i_{\mathrm{II}}(k)$; thus, $0 < O(t) < 1$.

3) When internal pole-to-pole faults occur, the topological symmetry of the transient system in such cases determines that $\Delta i_{\mathrm{I}}(k) \approx \Delta i_{\mathrm{II}}(k)$; thus, $O(t) \approx 1$.

In this paper, the pole selection subunit will recognize a detected fault as positive if the calculated $O(t)$ is larger than 1.5, or negative if $O(t)$ is less than 0.5. If $O(t)$ is between 0.5 and 1.5, the fault is classified as a pole-to-pole (PtP) fault. Only the protection of the faulted pole will be allowed to trip.

2) Reverse Fault Detection Subunit

When a reverse fault (taking the local protection installation as the point of reference) occurs, it is known from Section III that the fault-induced refracted TW will directly impact the local relay protection without the influence of the opposite line boundary and transmission line, which may partially induce the features of an internal fault in the local measurements and cause the protection to trip incorrectly.

The principle of reverse fault detection is relatively mature. According to the definition of the forward TW in (1), the direction of the current TW and the adopted convention for the local current measurement are the same in this context. Therefore, $\Delta I_{\mathrm{m}}(t)$ at the local terminal has a negative sign, which can be easily identified to classify the direction of the fault. On this basis, the following auxiliary criteria for the local differential current are constructed:

$$\Delta I_{\mathrm{m}}(t+t_0) = I_{\mathrm{m}}(t+t_0) - I_{\mathrm{m}}(t+t_0-1) \tag{43}$$

$$\Delta I_{\mathrm{m}}(t) > I_{\mathrm{Lset}} \tag{44}$$

where I_{Lset} is a small positive value set to prevent maloperation in the case of a reverse fault. The subunit continuously determines the magnitude of $\Delta I_{\mathrm{m}}(t)$ since the protection starts. The entire composite protection scheme should only be allowed to operate when $\Delta I_{\mathrm{m}}(t)$ is larger than I_{Lset}.

D. Overall Scheme

Figure 15 shows the overall scheme of the proposed single-end protection based on transient power waveshape for hybrid HVDC transmission lines. Its functional process is as follows.

1) When an abnormal TW front reaches the protection installation, the undervoltage/overcurrent criterion starts and provides protection during the operation. The reverse fault detection subunit then continuously monitors the value of $\Delta I_{\mathrm{m}}(t)$ and blocks any potential maloperation caused by the reverse faults.

2) The protection installation quickly calculates the floating threshold of the differential transient TW power based fault identification subunit using preset values and compares it with $|\Delta P_{\mathrm{m}}(t)|$ calculated point-by-point in real time to effectively reflect the internal line abnormalities and eliminate the influence of forward external faults.

3) Using (2), the maximum $P_{\mathrm{m}}(t)$ since the protection starts is calculated and updated point-by-point in real time, from which the per-unit transient power accumulation D_{A} is calculated and compared with the unit's threshold, effectively eliminating possible risk of maloperation induced by LD.

4) After the abnormal signal is recognized as an internal fault, the protection installation selects the faulty pole using $O(t)$ and trips if it is on the faulty pole.

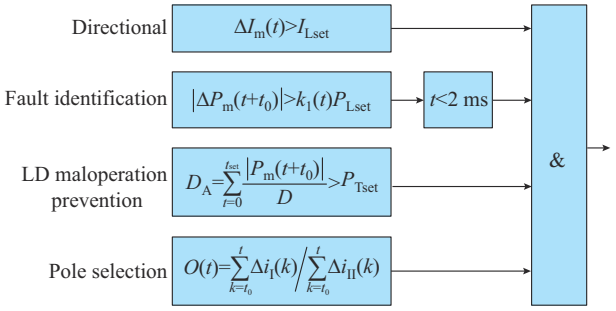

Fig. 15. Overall scheme of proposed single-end protection based on transient power waveshape for hybrid HVDC transmission lines.

V. Case Studies

This section presents case studies under various abnormal conditions to demonstrate the advantages of the proposed protection scheme. These case studies have been carried out with the 500 kV PtP hybrid HVDC transmission system in Fig. 1, emphasizing the scenarios involving an internal high-resistance grounding fault at F_4, a metallic grounding fault at F_5, and a lightning disturbance at F_5. The transmission system is modeled using RTDS with a sampling frequency of 20 kHz, and the OT of each subunit is calculated with the protection start-up point as the starting point.

A. Verification of Performance at VSC End

Figure 16 shows the waveforms of the local measurements at VSC end, including the measured P_{m}, ΔP_{m} and its floating threshold ΔI_{m}, and O under various abnormal conditions within 2 ms after the protection starts. Figure 16(a) shows that P_{m} under abnormal internal conditions quickly peaks at a relatively large value that would be recognizable even when the fault resistance R_{g} (if it exists) is up to 750 Ω, whereas P_{m} under external fault conditions smoothly varies within a limited range. Consequently, ΔP_{m} under abnormal internal conditions quickly exceeds the floating threshold, whereas ΔP_{m} under external fault conditions can never meet the floating threshold, as shown in Fig. 16(b). This indicates that the differential transient TW power based fault identification unit can reliably detect, identify, and roughly locate line abnormalities at the VSC end.

Figure 16(c) shows that the sign of ΔI_{m} is negative only under reverse fault conditions, through which the reverse fault detection subunit can easily flag a reverse line abnormality and operate accordingly. Figure 16(d) shows that O far exceeds 1 within 0.5 ms after the protection starts when any positive line abnormalities occur.

The performance of the LD maloperation prevention subunit can be verified by Fig. 17, in which the waveforms of the calculated D_{A} under the conditions of a 750 Ω PG fault (Fig. 17(a)) and lightning disturbance (Fig. 17(b)) at F_4 are presented. It can be observed that D_{A} during internal faults continuously increases at a steady slope, and then reaches the action threshold within 0.9 ms. The unit can then flag the detected line abnormality as a fault rather than LD. In

contrast, in Fig. 17(b), the transient power quickly peaks within 0.8 ms and then drastically declines to a very low level. Hence, D_A can never reach the action threshold, and the unit can then flag the abnormality as LD in this circumstance.

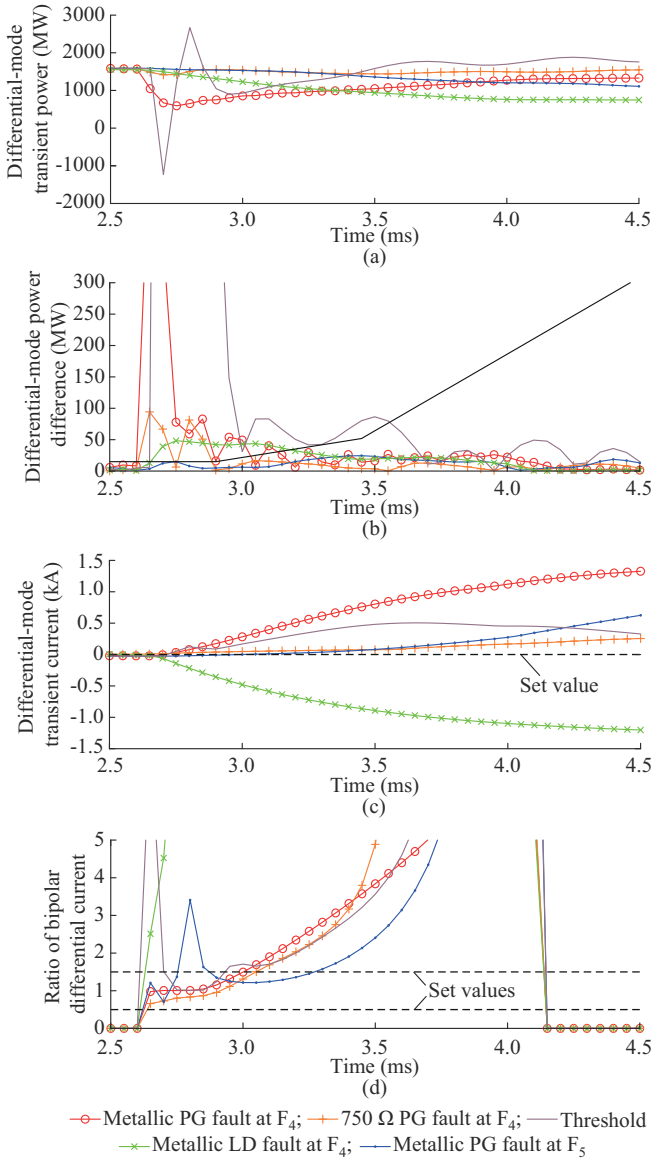

Fig. 16. Waveforms of local measurements at VSC end under different faults. (a) Differential-mode transient power. (b) Differential-mode power difference. (c) Differential-mode transient current. (d) Ratio of differential currents of both poles.

Table I summarizes the line protection OT in different abnormal scenarios at the VSC end of the hybrid system. The scheme can reflect various internal faults, with its OT reduced to within 1 ms while reliably blocking external faults and LD. It can also be used to sensitively identify PtP faults.

B. Performance Verification at LCC End

Likewise, when applied to the LCC end, the performance of the proposed protection scheme is sequentially verified by the subunits.

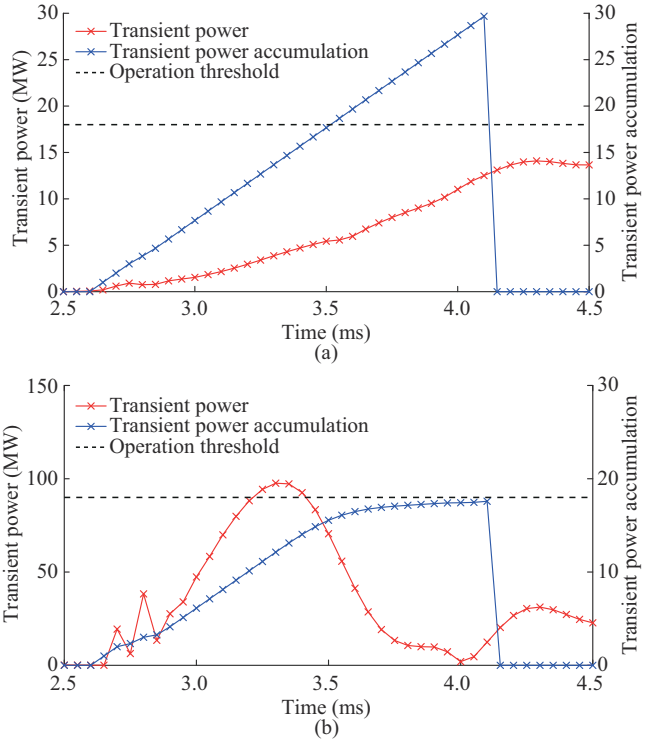

Fig. 17. Waveforms showing performance of LD maloperation prevention subunit. (a) During 750 Ω PG fault at F_4. (b) During LD at F_4.

TABLE I
LINE PROTECTION OT AT VSC END

Fault property	Startup time (ms)	OT (ms)		
		Section III-A	Section III-B	Total net
Metallic PG fault at F_2	0.1	0.1	1.0	0.9
Metallic PG fault at F_3	1.3	1.3	2.3	1.0
Metallic PG fault at F_4	2.6	2.6	3.5	0.9
750 Ω PG fault at F_2	0.1	0.1	1.0	0.9
750 Ω PG fault at F_3	1.3	1.3	2.3	1.0
750 Ω PG fault at F_4	2.6	2.6	3.6	1.0
Metallic PtP fault at F_2	0.1	0.1	1.0	0.9
300 Ω PtP fault at F_2	0.1	0.1	1.1	1.0
Metallic PtP fault at F_4	2.6	2.6	3.6	1.0
300 Ω PtP fault at F_4	2.6	2.6	3.6	1.0
Metallic PG fault at F_5	2.6	Blocked		
Metallic LD fault at F_2	0.1	0.1	Blocked	
Metallic LD fault at F_3	1.3	1.3	Blocked	
Metallic LD fault at F_4	2.6	2.6	Blocked	
Metallic PG fault at F_7	2.6	Blocked		

Figure 18 shows the waveforms of the local measurements at the LCC end, including the measured P_m, ΔP_m and its floating threshold ΔI_m, and O under various abnormal conditions within 2 ms after the protection starts. Figure 18(a) and (b) shows that ΔP_m under abnormal internal conditions quickly peaks with abrupt variation in P_m, which can be sensitively recognized when R_g (if it exists) is up to 500 Ω and even 750 Ω. Further, P_m under external fault condi-

tions smoothly varies within a limited range. Consequently, ΔP_m at the LCC end fluctuates in patterns similar to those at the VSC end. Figure 18(c) and (d) shows that the auxiliary units can correctly operate under various situations.

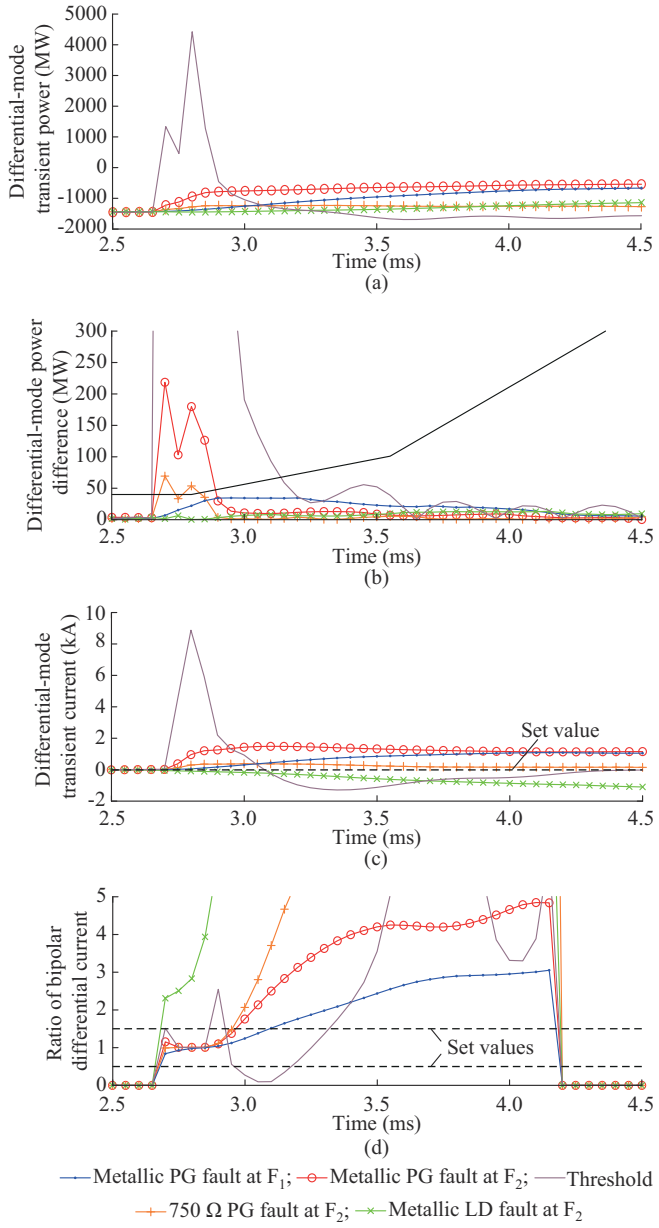

Fig. 18. Waveforms of local measurements at LCC end under different faults. (a) Differential-mode transient power. (b) Differential-mode power difference. (c) Differential-mode transient current. (d) Ratio of differential currents of both poles.

Figure 19 shows the performance of the LD maloperation prevention subunit under the conditions of a 750 Ω PG fault and LD at F_2. It can be observed that D_A in Fig. 19(a) can reach the action threshold in 0.85 ms. The subunit can then flag the detected line abnormality as a fault rather than LD, but D_A in Fig. 19(b) can never reach the action threshold.

Table II summarizes the line protection OT in different abnormal scenarios at the LCC end. This table shows that the proposed protection scheme is also applicable to the LCC ends.

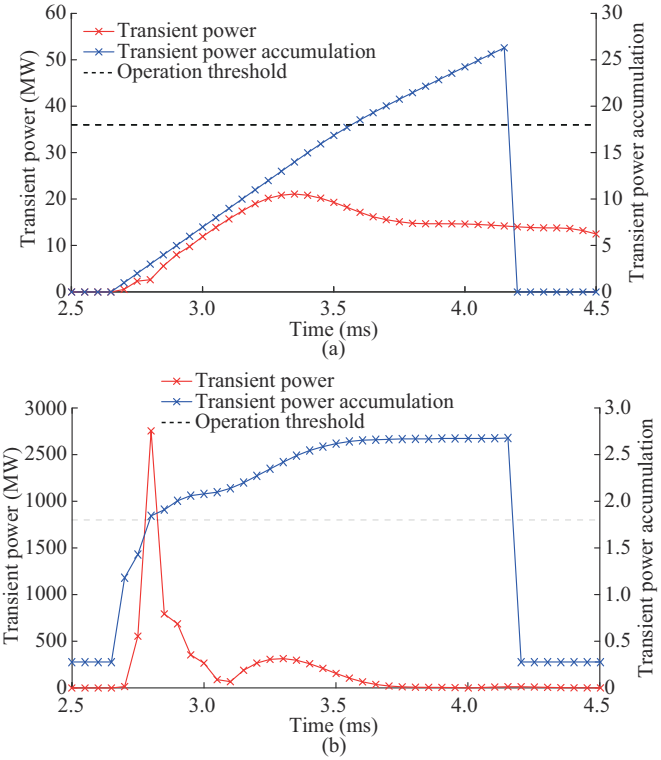

Fig. 19. Waveforms showing performance of LD maloperation prevention subunit. (a) During 750 Ω PG fault at F_2. (b) During LD at F_2.

TABLE II
LINE PROTECTION OT IN DIFFERENT ABNORMAL SCENARIOS AT LCC END

Fault property	Startup time (ms)	OT (ms)		
		Section III-A	Section III-B	Total net
Metallic PG fault at F_2	0.1	0.1	1.0	0.9
Metallic PG fault at F_3	1.3	1.3	2.2	0.9
Metallic PG fault at F_4	2.6	2.6	3.5	0.9
750 Ω PG fault at F_2	0.1	0.1	1.0	0.9
750 Ω PG fault at F_3	1.3	1.3	2.2	0.9
750 Ω PG fault at F_4	2.6	2.6	3.5	0.9
Metallic PtP fault at F_2	0.1	0.1	1.0	0.9
300 Ω PtP fault at F_2	0.1	0.1	1.0	0.9
Metallic PtP fault at F_4	2.6	2.6	3.6	1.0
300 Ω PtP fault at F_4	2.6	2.6	3.6	1.0
Metallic PG fault at F_5	2.6	Blocked		
Metallic LD fault at F_2	0.1	0.1	Blocked	
Metallic LD fault at F_3	1.3	1.3	Blocked	
Metallic LD fault at F_4	2.6	2.6	Blocked	
Metallic PG fault at F_6	2.6	Blocked		

C. Verification of Performance for Symmetric HVDC Transmission Systems

The proposed protection scheme might also be applied to symmetric HVDC transmission systems. As linearization methods can be applied to these systems to form linearized local systems with a similar topology, the performance of the proposed protection scheme should be further verified for such symmetric HVDC transmission systems.

1) Verification of a VSC-HVDC Transmission System

To verify the performance of the proposed protection scheme in standard symmetric VSC-HVDC transmission systems, the simplified Zhangbei four-terminal flexible HVDC transmission system of China in Fig. 20 is modeled. The model parameters can be found in [23]. In this paper, only the fault characteristics of the Zhangbei-Beijing transmission line are analyzed owing to space restrictions, and the Zhangbei terminal station is used as the local terminal.

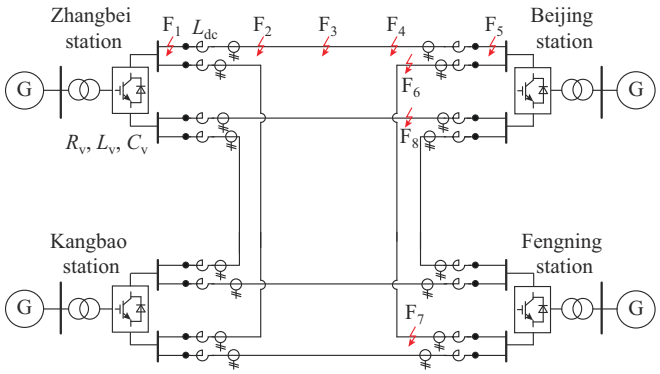

Fig. 20. Diagram of simplified Zhangbei four-terminal flexible HVDC transmission system of China.

The line protection OT of the proposed protection scheme in Zhangbei transmission system is summarized in Table III. The results indicate that the proposed protection scheme is applicable to VSC-HVDC transmission systems. As there is no DC filter at the line boundaries, the transient processes of the local measurements are shorter, and the operation of the proposed protection scheme is accelerated during internal faults. The scheme can reliably block out-of-zone faults and instantaneous disturbances. Specifically, it excels even more in reliability because the TWs induced by external line faults must first be buffered twice by the current-limiting reactors at opposite line boundaries before they can refract into the local transmission line.

TABLE III
LINE PROTECTION OT OF PROPOSED PROTECTION SCHEME IN ZHANGBEI TRANSMISSION SYSTEM

Fault property	Startup time (ms)	OT of Section III-A (ms)	OT of Section III-B (ms)	Total net OT (ms)
Metallic PG fault at F_2	0	0	0.5	0.5
Metallic PG fault at F_3	0.4	0.4	0.9	0.5
Metallic PG fault at F_4	0.7	0.7	1.2	0.5
750 Ω PG fault at F_2	0.1	0.1	0.6	0.5
750 Ω PG fault at F_3	0.4	0.4	1.1	0.7
750 Ω PG fault at F_4	0.7	0.7	1.4	0.7
Metallic PG fault at F_5	0.7	Blocked		
Metallic PG fault at F6	0.8	Blocked		
Metallic PG fault at F_7	1.7	Blocked		
Metallic PG fault at F_8	0.7	Blocked		
Metallic LD fault at F_2	0	0	Blocked	
Metallic LD fault at F_3	0.4	0.4	Blocked	
Metallic LD fault at F_4	0.7	0.7	Blocked	

2) Verification of an LCC-HVDC Transmission System

Using the parameters in Appendix A Tables AI and AII, the point-to-point symmetric LCC-HVDC transmission system in Fig. 21 is constructed. The line length in Fig. 21 is modified as 1500 km.

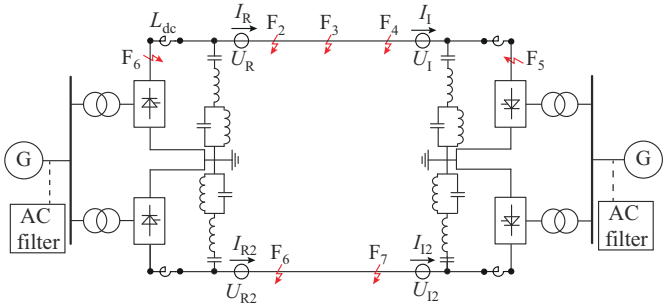

Fig. 21. Diagram of pole-to-pole symmetric LCC-HVDC transmission system.

The line protection OT of the proposed protection scheme in LCC-HVDC transmission system is summarized in Table IV. The results indicate that the proposed protection scheme can also be applied to LCC-HVDC transmission systems with superior performance.

TABLE IV
LINE PROTECTION OT OF PROPOSED PROTECTION SCHEME IN LCC-HVDC TRANSMISSION SYSTEM

Fault property	Startup time (ms)	OT (s)		
		Section III-A	Section III-B	Total net
Metallic PG fault at F_2	0.1	0.1	0.9	0.8
Metallic PG fault at F_3	2.6	2.6	3.6	0.9
Metallic PG fault at F_4	5.1	5.1	6.0	0.9
750 Ω PG fault at F_2	0.1	0.1	1.0	0.9
750 Ω PG fault at F_3	2.6	2.6	3.6	1.0
750 Ω PG fault at F_4	5.1	5.1	6.1	1.0
Metallic PtP fault at F_2	0.1	0.1	1.0	0.9
300 Ω PtP fault at F_2	0.1	0.1	1.0	0.9
Metallic PtP fault at F_4	5.1	5.1	6.2	1.1
300 Ω PtP fault at F_4	5.1	5.2	6.3	1.1
Metallic PG fault at F_5	5.6	Blocked		
Metallic LD fault at F_2	0.1	0.1	Blocked	
Metallic LD fault at F_3	2.6	2.6	Blocked	
Metallic LD fault at F_4	5.1	5.1	Blocked	
Metallic PG fault at F_7	5.1	Blocked		

VI. CONCLUSION

Through quantitative analyses of the formation process of local measurements in hybrid HVDC transmission systems, it is demonstrated that the waveshapes of the local measured voltage and current in the first few milliseconds after the arrival of a faulty TW are mainly determined by the topology of the local boundary. These features pose a severe challenge to the applicability of conventional DC line protection principles to hybrid HVDC transmission systems. However, DC filters hardly absorb the fault-induced TW energy, which

makes it feasible to design a proposed protection scheme suitable for hybrid HVDC transmission lines based on the variation in the local transient power.

This paper has proposed a single-end protection scheme to effectively detect, identify, classify, and locate line faults and disturbances in hybrid HVDC transmission systems by focusing on the waveshape of the local transient power. This protection scheme comprises four subunits that identify faults, distinguish disturbances, determine direction, and select poles with superior performance. Simulation results show that the proposed protection scheme can be applied to hybrid HVDC, symmetric VSC-HVDC, and conventional LCC-HVDC transmission systems with strong anti-interference ability and a sufficient sensitivity to identify internal faults with R_g up to 750 Ω in less than 1.5 ms.

The proposed protection scheme can be theoretically applied to DC transmission systems with terminal topologies similar to that in Fig. 1, and to diverse line structures. It is expected that the proposed protection scheme will be gradually expanded and applied to distribution networks with T-connection or multi-branch transmission lines in the future.

APPENDIX A

TABLE AI
LIST OF BASIC PARAMETERS OF VSC AND TRANSMISSION LINES

Converter parameter		Line parameter	
Item	Value	Item	Value
Number of submodules	240	Line length	800 km
Submodule resistance	0 Ω	Voltage level	500 kV
Submodule inductance	0.04 H	Inductance of L_{dc}	290 mH
Submodule capacitance	15000 μF	Conductor radius	0.018 m
Transformer primary voltage	525 kV	Conductor spacing	50 cm
Transformer secondary voltage	210 kV	Geometric center height of conductors	28 m
Transformer leakage reactance	0.18 p.u.	Geometric center width of conductors	8 m
Transformer capacity	892.5 MVA	Sag	14.9 m

TABLE AII
LIST OF BASIC PARAMETERS OF LCC AND DC FILTER

Converter parameter		DC filter parameter	
Item	Value	Item	Value
Transformer primary voltage	525 kV	$6^{th}/12^{th}$ filter H_{f1}	128 mH
Transformer secondary voltage	210 kV	$6^{th}/12^{th}$ filter C_{f1}	0.7 μF
Transformer capacity	892.5 MVA	$6^{th}/12^{th}$ filter H_{f2}	58.7 mH
Transformer leakage reactance	0.18 p.u.	$6^{th}/12^{th}$ filter C_{f2}	3.76 μF
Smooth inductance	290 mH	$6^{th}/12^{th}$ filter R_{f1}	1000 Ω

REFERENCES

[1] Y. Wang, W. Zhao, J. Yang *et al.*, "Hybrid high-voltage direct current transmission technology and its development analysis," *Automation of Electric Power Systems*, vol. 41, no. 7, pp. 156-167, Apr. 2017.

[2] Y. Liang, L. Jiang, H. Li *et al.*, "Fault analysis and traveling wave protection based on phase characteristics for hybrid multiterminal HVDC systems," *IEEE Journal of Emerging and Selected Topics in Power Electronics*, vol. 10, no. 1, pp. 575-588, Feb. 2022.

[3] M. Li, Z. Guo, D. Cai *et al.*, "Operating characteristic analysis of multi-terminal hybrid HVDC transmission system with different control strategies," in *Proceedings of 2018 International Conference on Power System Technology (POWERCON)*, Guangzhou, China, Nov. 2018, pp. 2616-2621.

[4] B. Xiang, J. Luo, L. Gao *et al.*, "Study on the parameter requirements for resistive-type superconducting fault current limiters combined with mechanical DC circuit breakers in hybrid AC/DC transmission grids," *IEEE Transactions on Power Delivery*, vol. 35, no. 6, pp. 2865-2875, Dec. 2020.

[5] S. Gao, X. Song, H. Ye *et al.*, "Single-end electrical quantity protection method suitable for hybrid bipolar DC system," *Journal of Xi'an Jiaotong University*, vol. 55, no. 7, pp. 79-87, Feb. 2021.

[6] M. Farshad, "A pilot protection scheme for transmission lines of half-bridge MMC-HVDC grids using cosine distance criterion," *IEEE Transactions on Power Delivery*, vol. 36, no. 2, pp. 1089-1096, Apr. 2021.

[7] J. Ma, Y. Wu, C. Liu *et al.*, "Pilot directional protection scheme for LCC-HVDC transmission lines based on the voltage difference between positive and negative poles," *IEEE Transactions on Power Delivery*, vol. 37, no. 2, pp. 696-709, Apr. 2022.

[8] L. Ning, N. Tai, X. Zheng *et al.*, "Research on MMC-HVDC transmission line protection scheme based on one-terminal transient current," *Proceedings of the CSEE*, vol. 37, no. 17, pp. 5010-5017, Jun. 2017.

[9] Z. Chen, Z. Zhou, X. Wang *et al.*, "Research on protection scheme of hybrid multi-terminal DC transmission lines," *Power System Technology*, vol. 43, no. 7, pp. 2617-2622, Jul. 2019.

[10] X. Yu and L. Xiao, "A DC fault protection scheme for MMC-HVDC grids using new directional criterion," *IEEE Transactions on Power Delivery*, vol. 36, no. 1, pp. 441-451, Feb. 2021.

[11] J. Zhou, C. Zhao, C. Li *et al.*, "Pilot protection method for DC lines based on included angle cosine of fault current component," *Automation of Electric Power Systems*, vol. 42, no. 14, pp. 165-171, Jul. 2018.

[12] L. Zhang, Y. Zhou, J. Yu *et al.*, "Modeling, control, and protection of modular multilevel converter-based multi-terminal HVDC systems: a review," *CSEE Journal of Power and Energy Systems*, vol. 3, no. 4, pp. 340-352, Dec. 2017.

[13] S. Yan and Y. Jiang, "Single-ended protection for flexible DC transmission line based on curvature of initial traveling wave," *Transactions of China Electrotechnical Society*, vol. 36, no. 9, pp. 1831-1841, Aug. 2021.

[14] Z. Chen, Z. Zhou, X. Wang *et al.*, "Traveling wave protection for hybrid HVDC transmission lines based on dual-tree complex wavelet transform," *Power System Technology*, vol. 43, no. 10, pp. 3832-3840, Jul. 2019.

[15] Y. Zhang, H. Wang, T. Li *et al.*, "Combined single-end fault location method for LCC-VSC hybrid HVDC transmission line," *Automation of Electric Power Systems*, vol. 43, no. 21, pp. 187-194, Aug. 2019.

[16] G. Sun, B. Shi, Y. Zhao *et al.*, "Research on the fault location method and protection configuration strategy of MMC based DC distribution grid," *Power System Protection and Control*, vol. 43, no. 22, pp. 127-133, Nov. 2019.

[17] X. Chen, H. Li, G. Wang *et al.*, "A convolution power-based protection scheme for hybrid multiterminal HVDC transmission systems," *IEEE Journal of Emerging and Selected Topics in Power Electronics*, vol. 9, no. 2, pp. 1655-1667, Apr. 2021.

[18] C. Zhang, J. Huang, G. Song *et al.*, "Non-unit ultra-high-speed line protection for multi-terminal hybrid LCC/MMC HVDC system and its application research," *IEEE Transactions on Power Delivery*, vol. 36, no. 5, pp. 2825-2838, Oct. 2021.

[19] L. Tang and X. Dong, "An approximate method for the calculation of transmission line fault current in MMC-HVDC grid," *Proceeding of the CSEE*, vol. 39, no. 2, pp. 490-498, Jan. 2019.

[20] L. Tang, X. Dong, S. Shi *et al.*, "Principle and implementation of ultra-high-speed travelling wave based protection for transmission line of flexible HVDC grid," *Power System Technology*, vol. 42, no. 10, pp. 3176-3186, Oct. 2018.

[21] W. Xiang, S. Yang, G. P. Adam *et al.*, "DC fault protection algorithms of MMC-HVDC grids: fault analysis, methodologies, experimental validations, and future trends," *IEEE Transactions on Power Electronics*, vol. 36, no. 10, pp. 11245-11264, Oct. 2021.

[22] H. Cao, Z. Zhou, H. Liu *et al.*, "A novel whole-line fast protection scheme based on single-ended current accumulation for HVDC transmission lines," *Proceeding of the CSEE*, vol. 41, no. 12, pp. 4091-4103, Nov. 2021.

[23] X. Yu, L. Xiao, L. Lin *et al.*, "Single-ended fast fault detection scheme for MMC-based HVDC," *High Voltage Engineering*, vol. 44,

no. 2, pp. 440-447, Feb. 2018.

Feiyang Dai received the B.Sc. degree in automation from Yanshan University, Qinhuangdao, China, in 2016, and the M.Sc. degree in electrical engineering from China Electric Power Research Institute (CEPRI), Beijing, China, in 2019. He is currently pursuing the Ph.D. degree in electrical engineering at the CEPRI, Beijing, China. His current research interests include DC power system protection and automation, mainly DC protection design and improvements using traveling wave signatures based techniques.

Zexin Zhou received the B.Sc. degree in relay protection & automatic remote from North China Electric Power University (NCEPU), Beijing, China, in 1991, and the M.Sc. degree in electric power system and its automatic from China Electric Power Research Institute (CEPRI), Beijing, China, in 1994. Currently, she is the Director of the Relay Protection Department of CEPRI, an Engineering Professor, and a Doctoral Supervisor. Her research interest includes relay protection of electric power systems.

Xingguo Wang received the B.Sc., M.Sc., and Ph.D. degrees from North China Electric Power University (NCEPU), Beijing, China, in 2003, 2006, and 2010, respectively. He is with Power System Dynamic Simulation Laboratory, China Electric Power Research Institute (CEPRI), Beijing, China. His research interests include relay protection algorithm and practice in power systems.